UNIVERSITY OF BRISTOL

Peer reviewed version

University of Bristol - Explore Bristol Research
General rights

AIAA 2023-xxxx

Local Analysis-Test Correlation of Tow-Steered Composite Shells with Small Cutouts

K. Chauncey Wu
NASA Langley Research Center
Hampton, Virginia

Rainer M.J. Groh
University of Bristol
Bristol, United Kingdom

Nathaniel W. Gardner
NASA Langley Research Center
Hampton, Virginia

**2023 AIAA Science and Technology
Forum and Exposition**
National Harbor, Maryland
23-27 January 2023

Local Analysis-Test Correlation of Tow-Steered Composite Shells with Small Cutouts

K. Chauncey Wu[1]
NASA Langley Research Center
Hampton, Virginia 23681

Rainer M. J. Groh[2]
Bristol Composites Institute
University of Bristol
Bristol BS8 1TR, United Kingdom

Nathaniel W. Gardner[3]
NASA Langley Research Center
Hampton, Virginia 23681

Abstract

The prebuckling and postbuckling behavior of two composite tow-steered shells with small cutouts is assessed using nonlinear dynamic finite element analyses and compared in detail with experimental measurements. The cylindrical shells were manufactured without cutouts using an automated fiber placement system, where the shells' fiber orientation angles vary continuously around the shell circumference from ±10 degrees on the axially stiff crown and keel, to ±45 degrees on the shear-stiff sides. The first shell with overlaps has laminate thickness variations on the crown and keel that result from application of all 24 tows during each pass of the fiber placement system. The second shell without overlaps uses the fiber placement system's tow drop/add capability to achieve a more uniform shell wall thickness. An unreinforced cutout representing a passenger door on a commercial aircraft fuselage is machined into the side of each of the two shells. These shells with cutouts were tested in axial compression and buckled elastically in previous work. Detailed nonlinear finite element analysis results are compared with their corresponding measured local load-displacement and load-strain responses in prebuckling, at global buckling, and into a stable postbuckled state. Test data from displacement transducers, strain gages, and digital image correlation are extracted at the centers of the crown and keel, and at the middles of the top and left edges of the cutout. The agreement between these measured and analytical local responses is excellent in prebuckling through global buckling, and very good from global buckling through postbuckling. As such, the excellent overall correlation observed here increases confidence in applying tow-steered composites in operational vehicles.

I. Introduction

Most practical aerospace vehicle structures include one or more cutouts of varying shapes and sizes. These common features are used for windows, payload deployment, or maintenance access, and can greatly affect the behavior of their surrounding structures under applied loads. State-of-

---

[1] Acquisition Manager, Science Office for Mission Assessments, AIAA Associate Fellow.

[2] RAEng Research Fellow, Lecturer in Digital Engineering of Structures, Department of Aerospace Engineering.

[3] Research Aerospace Engineer, Structural Dynamics Branch, Research Directorate.

the-art automated manufacturing techniques for modern composite structures (*e.g.*, fiber placement and continuous tow shearing; Refs. 1, 2) allow tailoring of the structural load paths around cutouts and other discontinuities (Refs. 3, 4). To increase confidence in their application to operational vehicles, the performance of these non-conventional composite structures must whenever possible be quantified using computational methods (typically finite element analyses [FEA]), and also validated from tests of scaled or full-size structures.

To further progress towards these goals, two cylindrical, unstiffened composite shells with tailored, tow-steered layups were designed (Ref. 5) and manufactured (Ref. 6) using an automated fiber placement system (AFPS). The shells with this pristine configuration (*i.e.*, without cutouts) were initially tested (Ref. 7) in end compression to deep postbuckling, with linear (Ref. 7) and nonlinear (Ref. 8) FEA performed to assess their complex structural behavior. After these tests were completed, nondestructive inspection indicated that the shells were undamaged, providing an opportunity to modify their configuration and gain additional insight into their structural behavior.

A small, unreinforced cutout was then machined into the center of one side of each shell. The cutout dimensions and orientation are approximately proportional to a commercial aircraft passenger door. End compression tests and linear FEA of these shells with small cutouts were performed (Ref. 9) to assess their load-end shortening structural responses. Recently, additional high-fidelity, nonlinear dynamic FEA of these shells with small cutouts were performed (Ref. 10) to better model their load-end shortening behavior, including the response into the deep postbuckling regime.

Quantitative comparisons of the analytical and experimental global load-end shortening structural responses were presented in Ref. 10 for the tow-steered composite shells with both small and large cutouts, along with qualitative comparisons of radial deflections from both FEA and global, full-field three-dimensional (3D) digital image correlation (DIC) data. The current study presents detailed local comparisons of the experimental and nonlinear analysis results at several selected locations on the shells with small cutouts. These results are plotted during prebuckling, at global buckling, and through stable postbuckling. Local measurements of displacements and in-plane strains were made using point-source instrumentation, and are compared against corresponding results extracted from analyses of the DIC data.

II. Tow-steered composite shells

Two right-circular composite cylinders with tow-steered layups, each nominally 35 inches in length with an inner diameter of 16.29 inches, were evaluated in this study. Both monocoque shells had the same nominal eight-ply $[\pm 45/\pm\Theta]_s$ layups, where the longitudinal fiber angle Θ varied continuously around a circular arc from 10 degrees on the shell crown and keel to 45 degrees on the shell sides (Ref. 5).

The shells were then manufactured using an AFPS from IM7/8552 prepreg slit tape with a nominal 0.0052-inch cured ply thickness (Ref. 6). The first shell with overlaps applied the full course of 24 tows during every pass of the AFPS. This resulted in overlapping tows being placed during fabrication, and local increases in shell wall thickness of up to a nominal 16-ply laminate on the crown and keel. The second shell without overlaps had a more uniform wall thickness caused by application of the AFPS's capability to cut and add tows during fabrication.

After completion of the initial testing of the pristine shells (Ref. 7), post-test nondestructive inspection using flash thermography showed that both shells were undamaged. No external signs of damage or material failure were observed on the shell surfaces. The shell configurations were then modified to introduce a rectangular cutout, providing a new structural configuration for additional studies.

This unstiffened, unreinforced cutout, shown in Fig. 1, was machined into the center of one side of each shell, where the nominal composite layup is approximately $[\pm 45]_{2s}$. This cutout size was selected to closely approximate the scaled dimensions of a passenger door on a commercial aircraft fuselage. The cutouts were approximately 3 inches high and 4.88 inches circumferentially, with 0.50-inch corner radii. These shells with small cutouts were then retested in axial compression, as shown in Fig. 1a. After testing of these shells with cutouts, the flash-thermography nondestructive inspection was repeated, which again showed the shells to be undamaged.
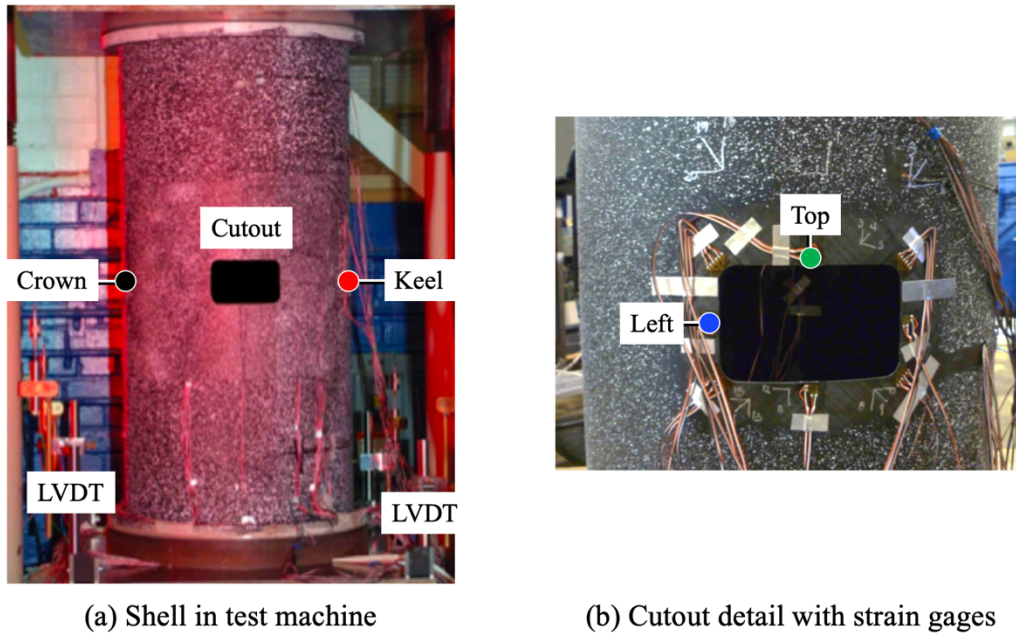

(a) Shell in test machine   (b) Cutout detail with strain gages

Figure 1. Tow-steered composite shell with small cutout

III. Test summary

These shells with small cutouts were loaded (Ref. 9) in end compression to global buckling using a computer-controlled displacement rate. The tests were stopped after global buckling, when a stable postbuckling equilibrium was achieved, and then the applied displacement was slowly removed until the shell axial load was approximately zero. The shell compression force was measured using a calibrated load cell permanently installed in the test machine and recorded using a digital data acquisition system.

Four linear variable displacement transducers (LVDTs), shown in Fig. 1a around the base of the shell, were used to measure the overall shell end shortening, with averaged results presented in Ref. 10. An LVDT was also installed to measure the cutout left edge radial deflection of the shell with overlaps. Back-to-back rosettes of electrical-resistance strain gages, shown in Fig. 1b, were bonded to the shell outer and inner surfaces before testing. These gages provided axial and transverse strain measurements at discrete locations around the cutout perimeter and over the shell acreage. LVDT and strain gage data were also recorded on the data acquisition system. Analog strain and displacement data were collected at 5 Hz during these shell tests.

Full-field digital image correlation (DIC) techniques were employed to provide a global assessment of the shells' structural response. During testing, high-resolution images were acquired using pairs of low-speed cameras in a stereo configuration at a rate of 1 Hz, and were postprocessed using the VIC-3D software (Refs. 11, 12) from Correlated Solutions, Inc. These cameras were

positioned to view the outer surfaces of both shells' cutout side and crown (assigned to the left of the cutout) during compression testing (see Fig. 2 below). Prior to installation into the test machine, a speckle pattern, shown in Fig. 1, was manually applied to the shells using white paint over a black base coat to provide high-contrast patterns for the DIC imaging process.

Qualitative color contour plots of radial deflections were generated over the camera view areas through post-test DIC image processing with the VIC-3D software, as shown in Ref. 10. Quantitative DIC values of radial deflections, axial strains, and transverse strains were also extracted at four locations on the shell outer surface for this study. These locations are shown in Fig. 2 as the filled circles and correspond to point-source measurements from strain gages and an LVDT, thus allowing direct comparisons to be made with DIC and analysis results.

During postprocessing, "noise floors" for the DIC deflections and strains were calculated with the VIC-3D software. These noise floors are estimates of the ±3-standard deviation statistical random errors of the respective deflections or strains. Estimated noise floors for each DIC camera pair are computed from time-averaged imagery taken without applied loads and are presented and discussed below.

Displacements and strains were recorded at rates of 1 to 5 Hz during these shell tests, which is a very low rate to capture the highly dynamic transition from global buckling to stable postbuckling. Despite the relative paucity of data and lower expectations for correlation in this loading regime, the analytical and measured strains and displacements are presented and discussed to provide additional insights into the shell behavior in this relatively unexplored region.
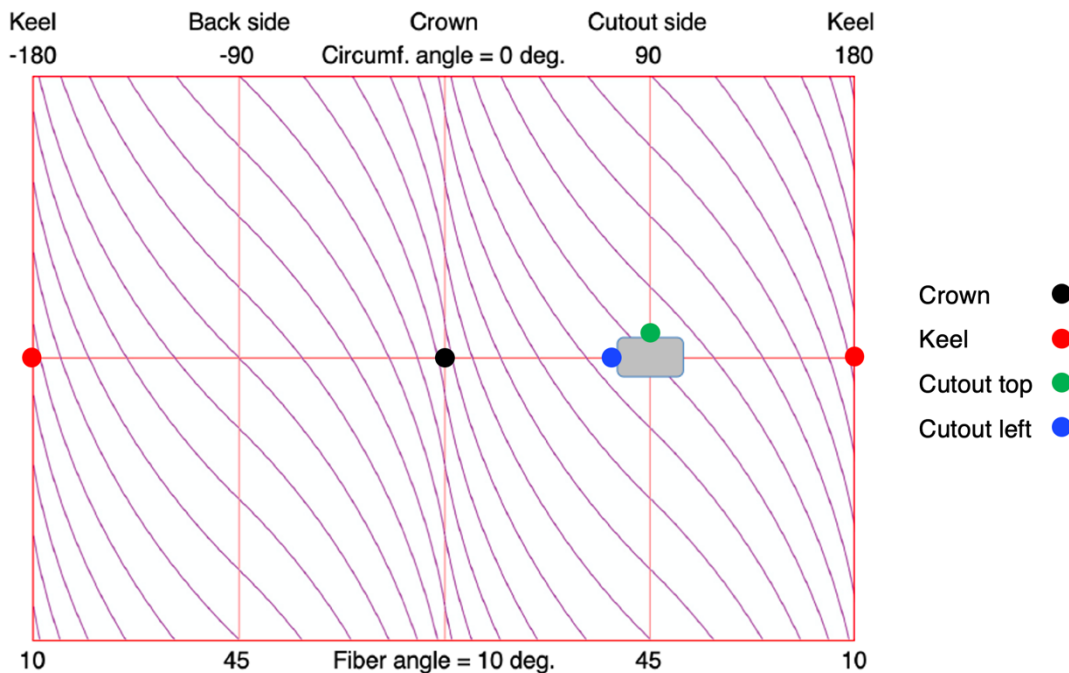

Figure 2. Shell planform with point measurement locations

IV. Analysis summary

Compression tests of the shells with small cutouts were originally supported with linear FEA (Ref. 9) to assess their buckling and axial stiffness. To complement these earlier studies, nonlinear dynamic FEA of these shells with small cutouts were performed (Ref. 10) recently. These higher-fidelity analyses provided quantitative comparisons of the measured and analytical shell load-end

American Institute of Aeronautics and Astronautics

shortening responses, as well as qualitative images of the shell radial deflections at both global buckling and stable postbuckling.

The Abaqus 2018 commercial FEA software (Ref. 13) was used to prepare converged analysis models of the shells with small cutouts, and to generate the analysis results for Ref. 10 and the present study. Full descriptions of these high-fidelity analyses and models are provided in Ref. 10 and are not repeated here. Nodal strains are computed using averaged centroidal values from the four elements surrounding each node. These node locations again correspond to the LVDT and strain gage locations described above.

As described in Ref. 10, the FEA results in this study are extracted from a dynamic analysis with geometric nonlinearities, but without material nonlinearities. During these analyses, the maximum end shortening achieved during the test is applied and removed as a constant-rate, bilinear ramp over 1200 seconds. The prebuckling regime is defined from zero load up to the maximum, global buckling load, where the shell end shortening drops sharply, which closely matches the physics of the experimental setup described above.

As the nonlinear analysis transitions past global buckling and seeks a stable postbuckled state (Ref. 14), significant variations are noted in the axial compression load, axial end shortening, radial deflections, and strains. The stable postbuckling load is defined as the axial force where the shell end shortening begins to monotonically decrease from its value at global buckling, and the effects of the dynamic transition from global buckling have dissipated. Qualitative trends in these terms, observed as the analysis develops, are compared with corresponding measured data.

V. Shell with overlaps

The measured and analytical structural responses of the shell with overlaps and a small cutout are plotted and discussed in this section. These comparisons are made at the center of the shell crown, and at the middle of the top and left edges of the cutout (Fig. 2). Where relevant, selected results are also presented at the center of the shell keel, with similarities and differences discussed in detail in the associated text. LVDT radial deflections were only measured at the middle of the cutout left edge for this shell.

For the present study, a reduced analysis step size was used to generate refined results near global buckling, with the resulting analytical prebuckling and postbuckled load-end shortening paths matching the nonlinear analysis results reported in Ref. 10. The prebuckling path was linear up to global buckling, with a global buckling load of 32,900 lbf at an end shortening of 0.067 inches. The refined analysis in this study converged to a stable postbuckling load of 23,340 lbf, which was close to the measured postbuckling load of 20,020 lbf. The qualitative nonlinear end shortening from this refined analysis also matches well with the experimental results as the stable postbuckling load is relieved and returns to zero.

A. Crown and keel centers

Color contour plots of the nonlinear FEA and experimental DIC radial deflections around the crown of the shell with overlaps are plotted at global buckling and stable postbuckling in Fig. 3. These full-field results are extracted from figures in Ref. 10, and represent relative, not absolute, quantifications. The red colors indicate the largest (most positive) outward displacements, and the dark blue color in the FEA and magenta color in the DIC indicate the smallest (most negative) inward displacements of the shell wall. While the relative areas within the FEA and DIC images are only approximately equal (due to a lack of physical reference marks on the shell), these results

agree very well on a qualitative basis, and illustrate the significant changes in displacements between global buckling and stable postbuckling.

Noise floors were computed and are presented here for the crown DIC measurements on both the shells with and without overlaps. The noise floor for deflections normal to the shell surface is ±0.001 inches, which is approximately one-third of the thickness of a sheet of paper. The noise floor for the in-plane deflections is one-half of this reported normal value for all of the DIC systems. The maximum in-plane strain noise floor for the axial and transverse strains is ±0.125 millistrain.
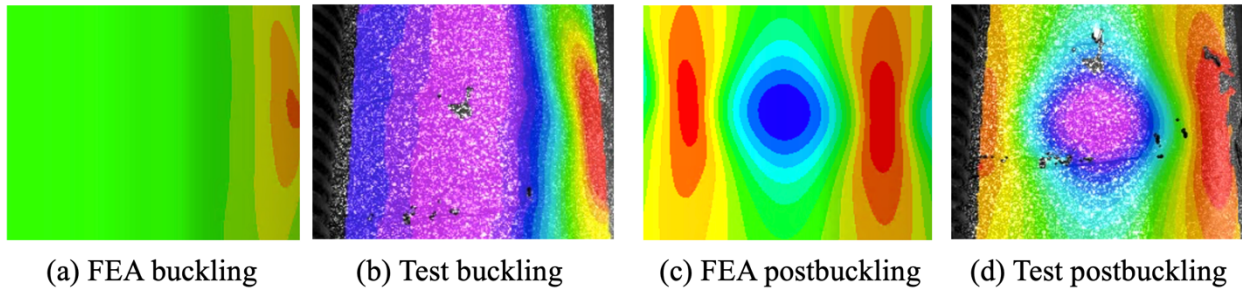

| (a) FEA buckling | (b) Test buckling | (c) FEA postbuckling | (d) Test postbuckling |

Figure 3. Full-field radial deflections around crown

1. Radial deflections

The radial deflections at the center of the crown of the shell with overlaps are plotted versus the axial compression load in prebuckling up to global buckling in Fig. 4a. Displacements are plotted for the nonlinear FEA and compared with the corresponding results extracted from full-field DIC measurements on the shell outer surface. The keel analytical prebuckling deflections were identical to the crown results shown here, however no DIC systems were positioned to view the keel.
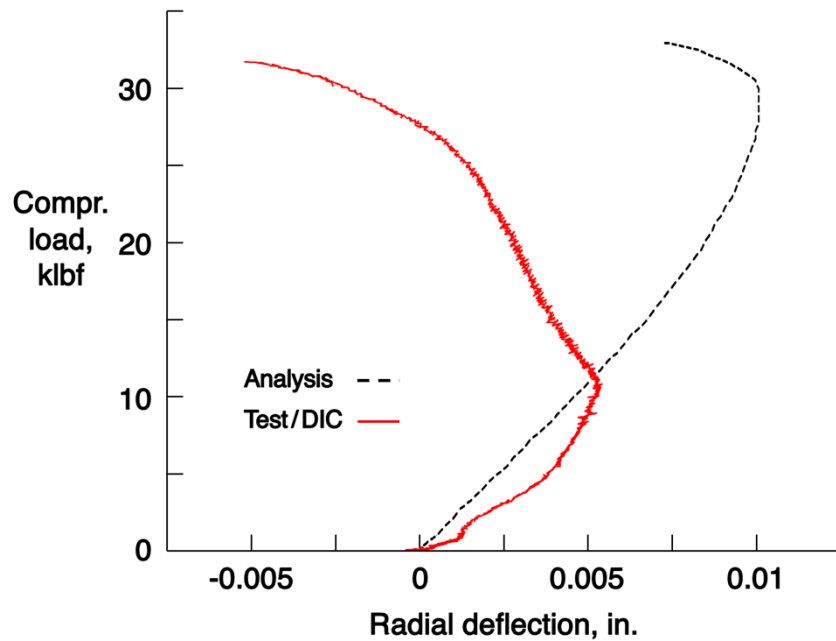

Figure 4a. Prebuckling deflections at crown center

American Institute of Aeronautics and Astronautics

Qualitatively, these local FEA and DIC displacements agree well with the global results in Figs. 3a and 3b, respectively. The point measurements differ slightly at loads below about 10 klbf, and the results then diverge rapidly with degraded correlation as the axial load increases. At best, the overall qualitative correlation is fair, and the quantitative agreement across these results is poor. These prebuckling deflections are on the order of the corresponding DIC noise floor, and therefore the lower bound of resolution for these DIC displacement measurements.

Postbuckling deflections at the centers of the crown and keel of the shell with overlaps are plotted versus axial compression load between global buckling and stable postbuckling in Fig. 4b. Results from the nonlinear FEA are plotted and compared with displacements extracted from full-field DIC measurements on the shell crown outer surface. The postbuckling results are denoted here and in the plots below using heavier line weights; the prebuckling deflections from Fig. 4a are also shown with lighter line weights for reference.
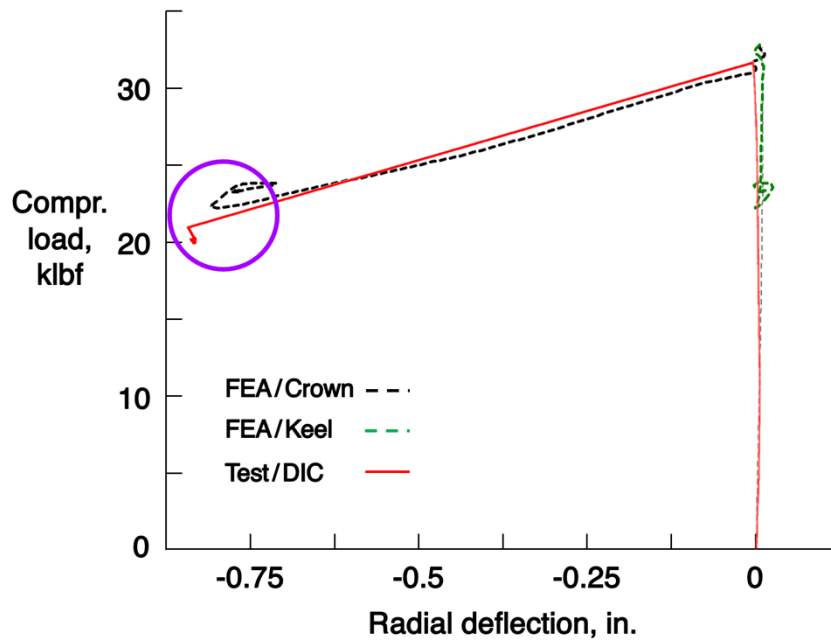

Figure 4b. Postbuckling deflections at crown and keel centers

While the predicted crown and keel prebuckling results were identical, the postbuckling radial deflections at those locations are very different. The analytical displacements on the shell crown, designated as the black dashed line, rapidly grow inwards to a maximum amplitude of approximately 0.75 inches. However, the keel postbuckling deflections, designated as the green dashed line, remain small as the axial load decreases.

The qualitative trends in these local FEA and DIC displacements at the shell crown align well with the full-field postbuckling results in Figs. 3c and 3d, respectively. The qualitative correlation between the postbuckling paths is very good, and the quantitative agreement between the final displacements at the stable postbuckled state (indicated within the purple circle) is excellent. Overall, the qualitative and quantitative agreement across these results is excellent.

2. Axial and transverse strains

The axial and transverse strains at the centers of the crown and keel of the shell with overlaps are plotted versus axial compression load in this section. Shell crown strains from prebuckling to global buckling from the nonlinear FEA are compared in Fig. 5a with corresponding results

extracted from full-field measurements on the shell outer surface using the VIC-3D software, as well as back-to-back point measurements from strain gages.

All of the strains in this figure are highly linear up to global buckling, and only become slightly nonlinear at higher loads, indicating that local bending is just starting to take place. Minimal differences between back-to-back strains are observed (*i.e.*, minimal axial and transverse bending) for both analysis and test results. Coefficients of variation (defined as the standard deviation divided by the mean value) computed for the linear best-fit slopes are 5.6 and 10.7 percent for the axial and transverse strains, respectively.

Excellent correlation is observed across these strain results from analysis and experimental methods at the shell crown. The keel prebuckling analysis results and the experimental strains from those strain gages are nearly identical to the crown results reported in Fig. 5a. These keel prebuckling strains are plotted in Fig. 5d with their corresponding postbuckling strains.
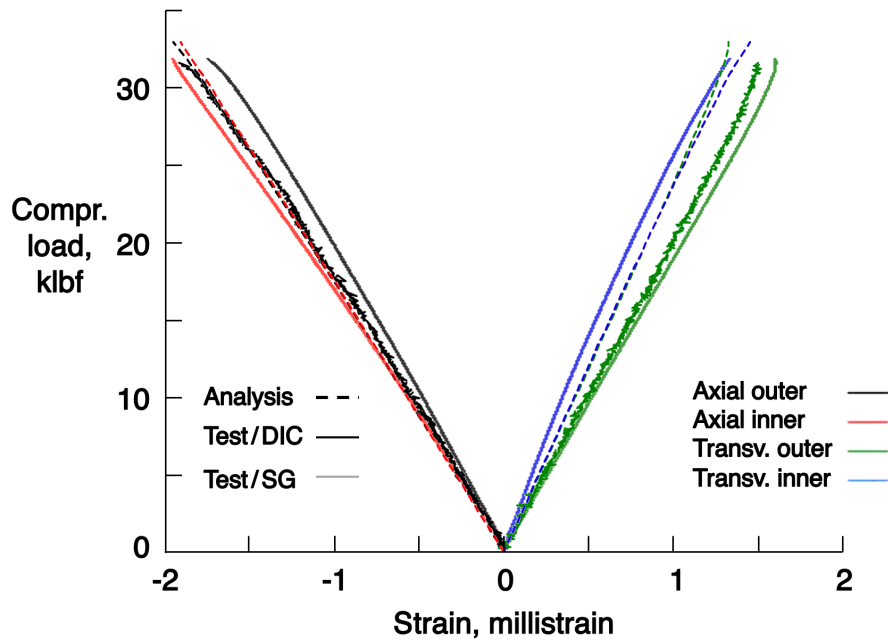

Figure 5a. Prebuckling strains at crown center

Nonlinear FEA and DIC strain measurements at the center of the shell with overlaps' crown are plotted in Fig. 5b. Axial and transverse outer surface strains (the black and green lines, respectively) are plotted versus axial compression load between global buckling and the stable postbuckling load in this figure. As in Fig. 4b, the postbuckling and prebuckling values are shown with heavier and lighter line weights, respectively. For clarity, only the outer surface strains are shown, and the inner surface strains are omitted. The postbuckling behavior of the DIC strains matches well with the trends in the FEA results, with excellent agreement in the final strains at the stable postbuckling load shown within the purple circle.

While the experimental and analytical DIC postbuckling strain paths plotted below are different, their qualitative correlation is still very good, as they both rapidly become more negative before equilibrating at the stable postbuckling load. The quantitative agreement between the final displacements at the stable postbuckled state (indicated within the purple circle) is excellent. Overall, the qualitative and quantitative agreement between these strains is excellent.

Nonlinear FEA and strain gage measurements at the centers of the shell with overlaps' crown and keel are plotted in Figs. 5c and 5d, respectively. Back-to-back axial and transverse strains are

American Institute of Aeronautics and Astronautics

plotted versus axial compression load between global buckling and the stable postbuckling load in these figures. The axial and transverse strains at the center of the shell with overlaps' crown, shown in Fig. 5c, are high at stable postbuckling. The average of the inner and outer surface axial strains from both test and analysis are close to zero at postbuckling, which corresponds well with the theoretical prediction of low in-plane loading in the postbuckled shell wall. The corresponding average transverse strains are approximately –1.2 to –1.5 millistrain, suggesting that some residual circumferential membrane compression remains after buckling.
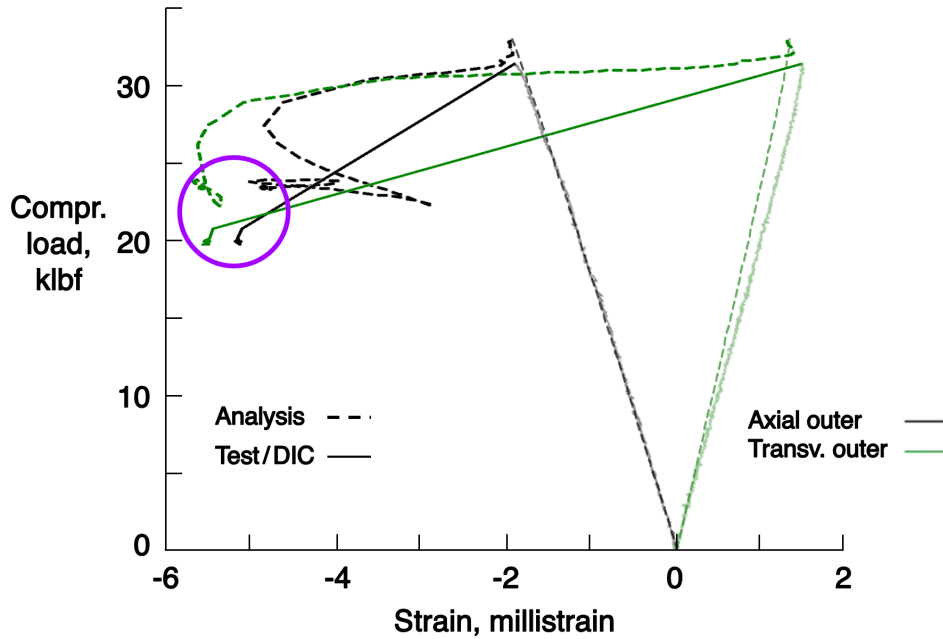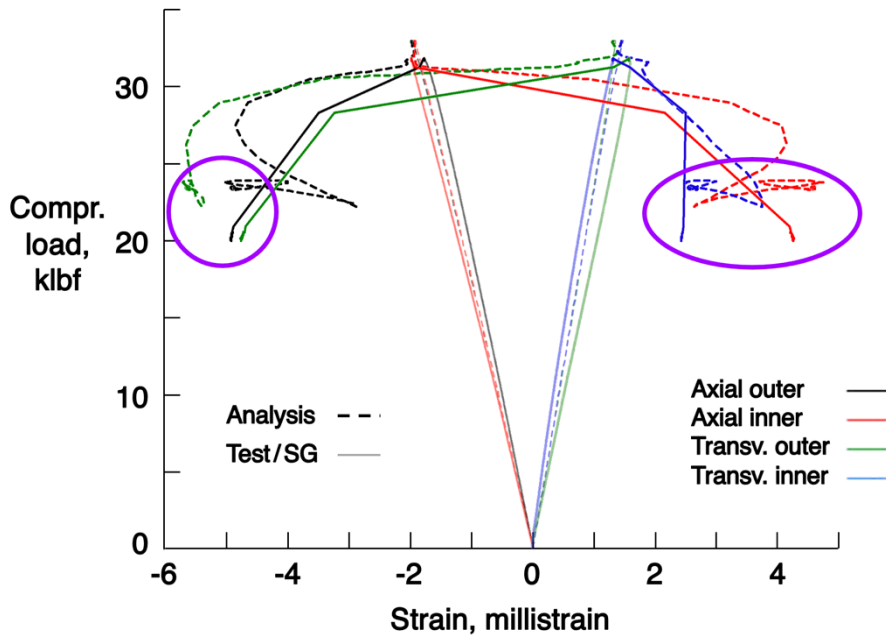

Figure 5b. Postbuckling DIC strains at crown center

Figure 5c. Postbuckling gage strains at crown center

American Institute of Aeronautics and Astronautics

The large differences between the outer- and inner-surface postbuckling strains at the center of the shell with overlaps' crown indicate that significant bending has taken place around both the shell's axial and transverse axes at that location. This result also implies the presence of large radial deflections at the shell crown center, which correspond well with the deflections noted in Fig. 4b above. Both the postbuckling paths and strains at the stable postbuckling loads agree very well, as indicated by the purple circles. Therefore, the qualitative and quantitative agreement across these results is excellent.

In comparison to the crown results plotted above, the axial and transverse strains at the center of the shell with overlaps' keel, shown in Fig. 5d, remain nearly constant as the axial load drops from global buckling to stable postbuckling. The average measured and analytical postbuckling strains at the shell keel are large, with amplitudes of 1.2 to 2 millistrain. This result suggests that the local membrane stresses in the shell wall are still high after global buckling.
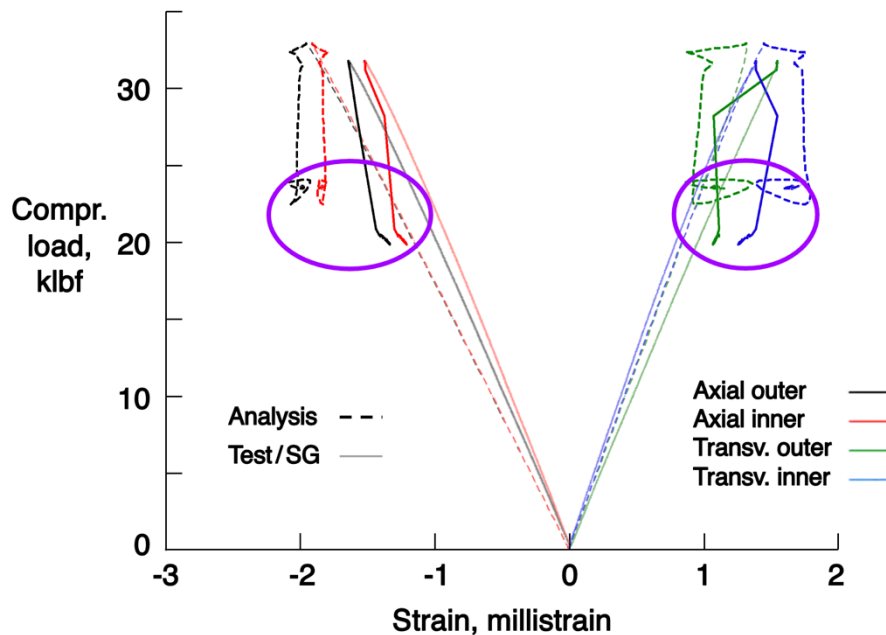

Figure 5d. Postbuckling gage strains at keel center

The back-to-back strain differences in Fig. 5d are very small, indicating that minimal local bending has happened within the shell wall after buckling. This result also suggests very little postbuckling radial deflection at this location, which corresponds well with the keel FEA results in Fig. 3b. The qualitative and quantitative agreement between analytical and experimental results, indicated by the purple circles, is excellent. As mentioned above, no DIC data were acquired at the shell keel center.

B. Cutout top edge

Color contour plots extracted from Ref. 10 of the nonlinear FEA and experimental DIC radial deflections around the cutout of the shell with overlaps are plotted at global buckling and stable postbuckling in Fig. 6. Unlike for the crown images in Fig. 3, the areas in these images are nearly equal since the reference dimensions are provided by the cutouts themselves. These results agree very well on a qualitative basis, with very minor differences. For example, the slight inward bulge on the right-hand side of the postbuckled image is below the cutout in Fig. 6c, and above the cutout in Fig. 6d. Significant changes in the radial displacements occur during the short time interval

between global buckling and stable postbuckling. The computed DIC noise floor around the cutout on the shell with overlaps is ±0.002 inches for the normal deflections. The maximum in-plane strain noise floor for the axial and transverse strains is ±0.550 millistrain.
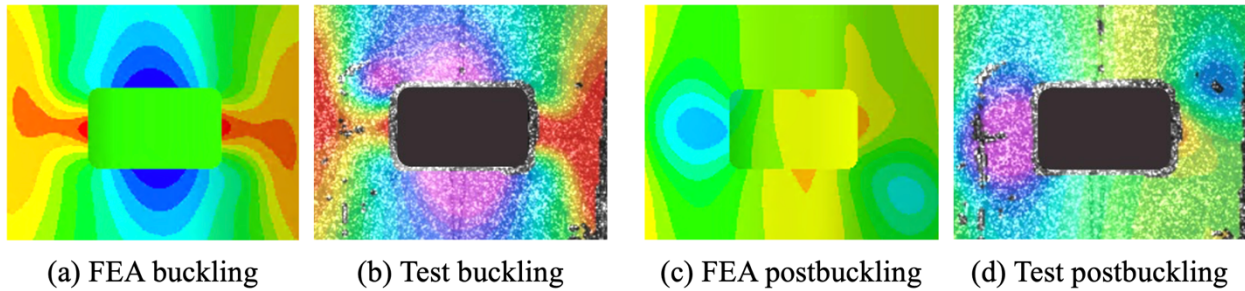

(a) FEA buckling   (b) Test buckling   (c) FEA postbuckling   (d) Test postbuckling

Figure 6. Full-field radial deflections around cutout

1. Radial deflections

The nonlinear FEA and experimental DIC radial deflections at the middle of the cutout top edge of the shell with overlaps are plotted versus axial compression load in prebuckling up to global buckling in Fig. 7a. These results agree well qualitatively with the buckling results in Fig. 6, with the displacements becoming increasingly negative as the axial load increases. Quantitatively, there are small differences at lower loads, with larger differences at higher loads as the shell approaches global buckling. Maximum deflection amplitudes of approximately 0.17 inches are 3.5 percent of the cutout width. Overall, the correlation across these results is very good.
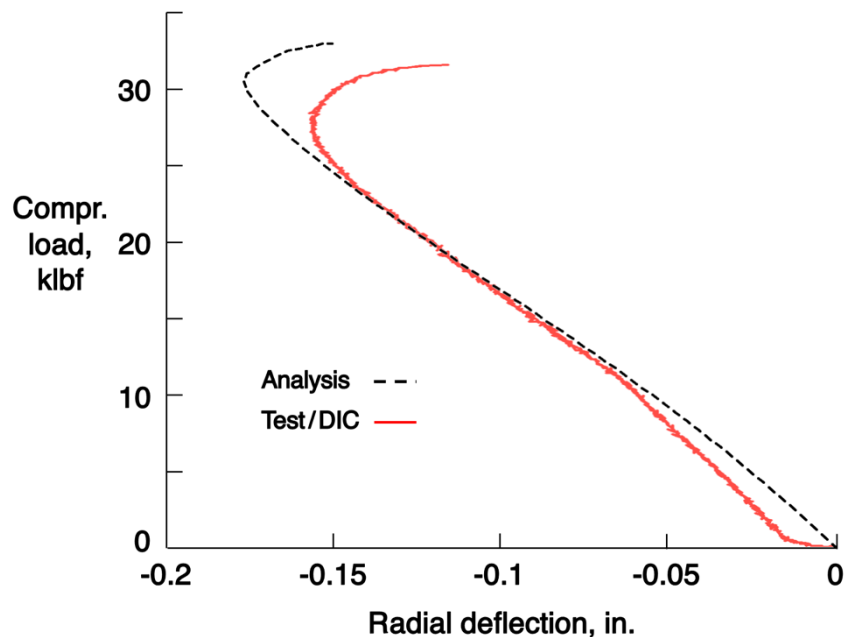

Figure 7a. Prebuckling deflections at cutout top edge

The corresponding radial deflections at the shell with overlaps cutout top edge are plotted versus axial compression load between global buckling and stable postbuckling in Fig. 7b. A qualitative comparison of the analytical and experimental postbuckling radial deflection paths plotted here show good correlation immediately after global buckling, as indicated by the dashed

purple circle. Qualitatively, both analytical and measured deflections increase from their values at global buckling, and approach zero at stable postbuckling, in agreement with the postbuckling results in Fig. 6. However, the final displacements at the stable postbuckling load show poor qualitative agreement, with fair overall agreement across these postbuckling results.
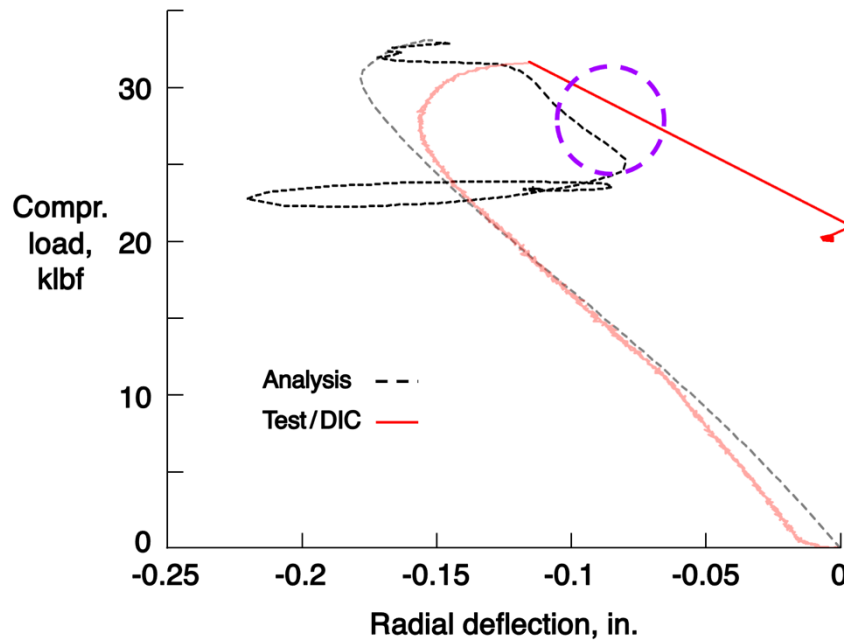

Figure 7b. Postbuckling deflections at cutout top edge

2. Axial and transverse strains

The nonlinear FEA and back-to-back gage axial and transverse strains at the middle of the cutout top edge of the shell with overlaps are plotted in prebuckling up to global buckling versus axial compression load in Fig. 8a. The averages of the back-to-back strains, and therefore the in-plane membrane loads, are very small across the entire load range. No DIC strain measurements are presented here due to poor correlation with the FEA and strain gage cutout results, and is attributed to boundary/edge effects, strain gage wire bundle interference, lighting, and speckle pattern size and density.

The strains shown are also highly nonlinear, with increasing differences between the outer and inner surface strains indicative of increasing bending with increasing load. As the axial load approaches global buckling, these strains then begin to converge. Overall, the correlation across these different results is very good to excellent. The analytical prebuckling strains at the middle of the cutout bottom edge are identical to the FEA results, and the corresponding experimental data are very similar to these test results but are not presented here. DIC strains around the cutouts are not presented because they showed poor correlation with the strain gage and FEA results, as mentioned above.

The corresponding axial and transverse strains on the shell with overlaps cutout top edge are plotted between global buckling and stable postbuckling in Fig. 8b. The postbuckled back-to-back strain pairs show large differences, indicating that significant bending has taken place around both the axial and transverse axes. While the magnitudes of these results are in rough agreement, they have opposite signs. This indicates that the measured and analytical shell walls are bending in opposite directions. Therefore, the overall qualitative and quantitative agreement between these postbuckling results is poor.
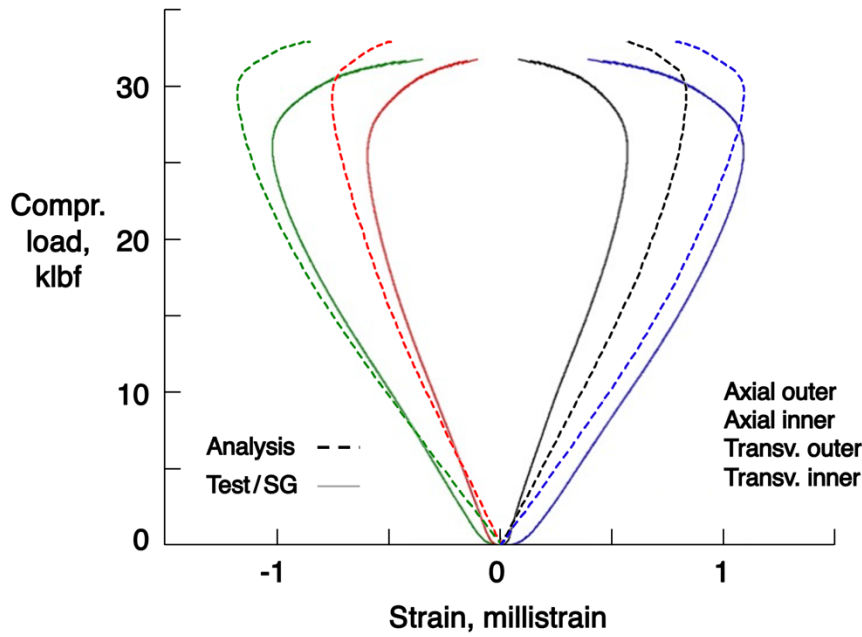
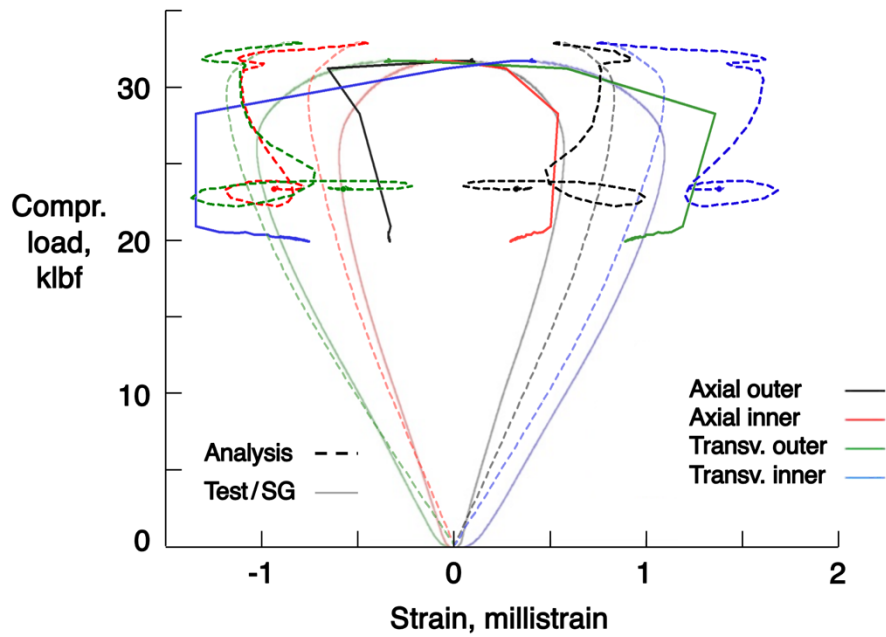**Figure 8a. Prebuckling strains at cutout top edge**

Figure 8b. Postbuckling strains at cutout top edge

C. Cutout left edge

1. Radial deflections

The radial deflections at the middle of the cutout left edge of the shell with overlaps are plotted versus axial compression load in prebuckling up to global buckling in Fig. 9a. Results are plotted here for the nonlinear FEA, test data from an LVDT installed at this location, and displacements extracted from full-field DIC measurements on the shell outer surface. The qualitative and quantitative correlation across these results is excellent, with all displacements increasing as the axial load increases.

The LVDT and DIC measurements are almost identical as the shell axial load approaches global buckling, reaching a maximum value of approximately 0.15 inches or approximately 5 percent of the cutout's 3-inch axial dimension. The maximum FEA deflection is approximately 0.020 inches greater than the corresponding measured results. Overall, the qualitative and quantitative agreement between the analytical and experimental deflections is excellent.
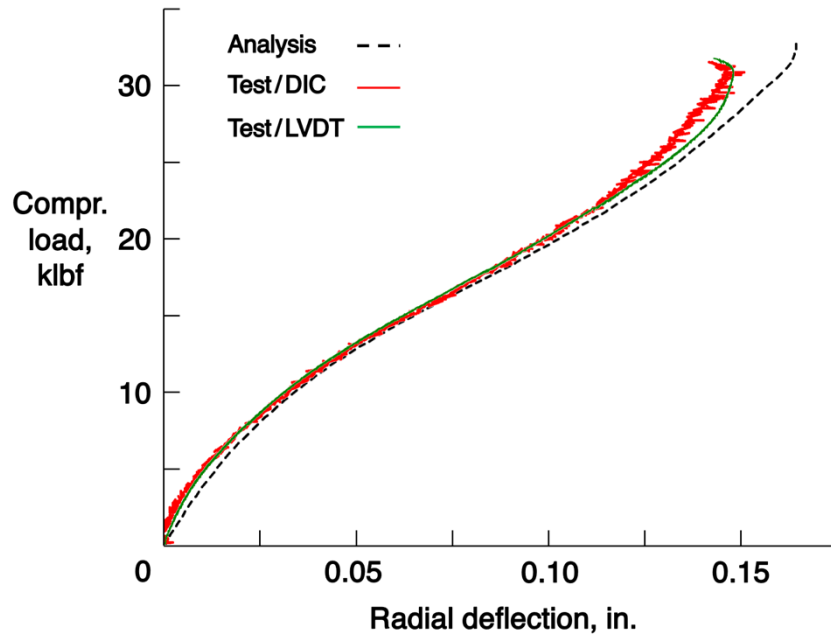

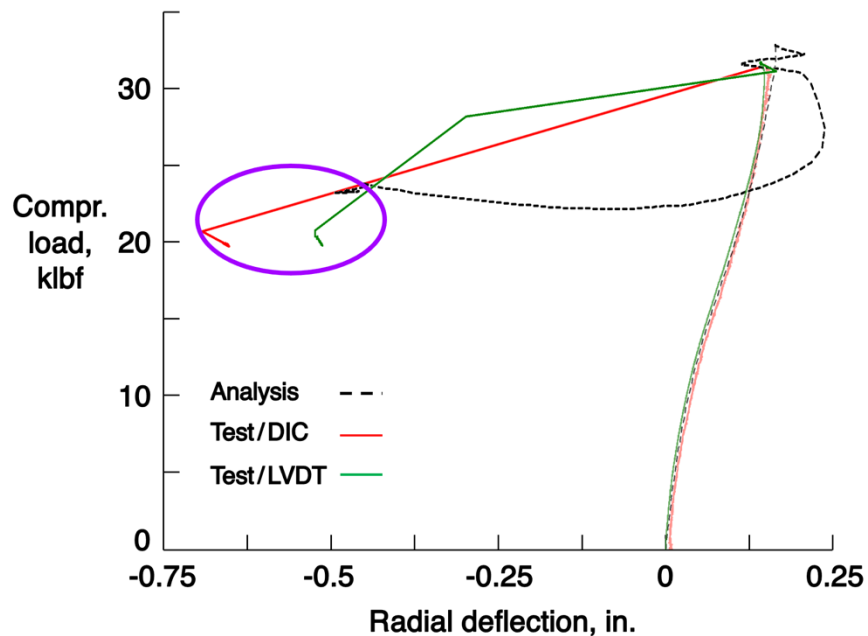**Figure 9a. Prebuckling deflections at cutout left edge**

Figure 9b. Postbuckling deflections at cutout left edge

The postbuckling radial deflections at the cutout left edge of the shell with overlaps between global buckling and stable postbuckling are plotted against load in Fig. 9b. Qualitative comparison

of the analytical and experimental postbuckling radial deflection paths plotted here show very good correlation after global buckling. The analytical and measured (both from LVDT and DIC) deflection amplitudes increase from their values at global buckling. They become increasingly negative, with very good qualitative agreement between these displacements at the stable postbuckling load. The average postbuckling radial deflection is almost 20 percent of the 3-inch cutout height. Overall, the qualitative and quantitative agreement across these results is assessed to be very good.

2. Axial and transverse strains

The nonlinear FEA and back-to-back gage axial and transverse strains at the middle of the cutout left edge of the shell with overlaps are plotted in prebuckling up to global buckling versus axial compression load in Fig. 10a. In comparison to the small (1 millistrain amplitude) values at the cutout top, the averaged strain magnitudes at the cutout edge steadily increase to about 5 to 6 millistrain at global buckling, with a maximum compressive strain of −14 millistrain.
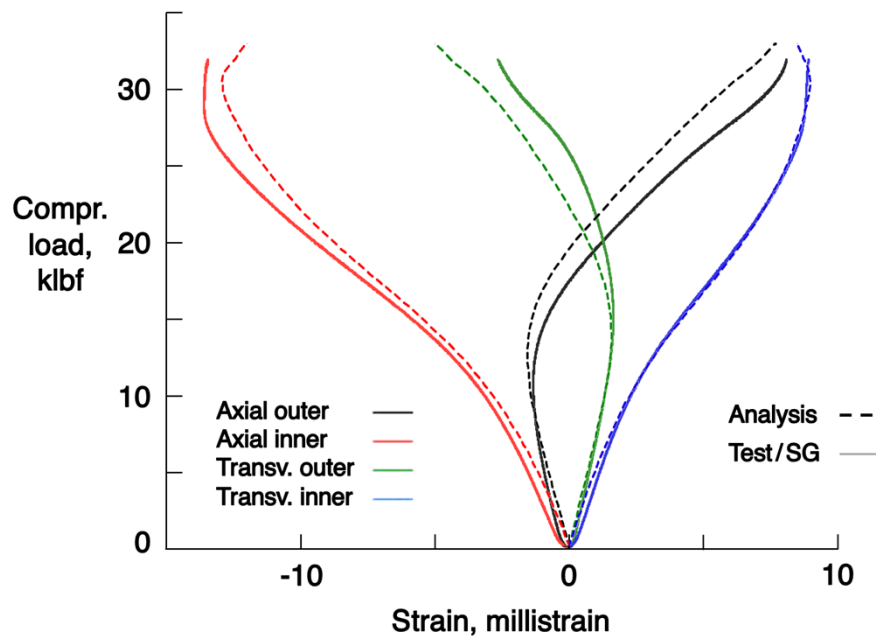

Figure 10a. Prebuckling strains at cutout left edge

The strains shown are also highly nonlinear, with increasing differences between the back-to-back strain pairs indicative of increasing through-thickness bending as the shell axial load also increases. Overall, the correlation across the strain results at this shell location is very good to excellent. Although not presented here to avoid duplication, the analytical prebuckling strains at the middle of the cutout right edge are identical to the FEA results plotted below for the cutout left edge, and the corresponding strain gage data at that location are also qualitatively very similar to the test results shown in the figure below.

Axial and transverse strains on the shell with overlaps cutout left edge are plotted versus axial compression load between global buckling and stable postbuckling in Fig. 10b. Results are only shown for the nonlinear FEA and back-to-back strain gage measurements on the shell outer surface. The measured strains on the shell inner surface (the red and blue lines in Fig. 10a) go rapidly off-scale high after global buckling, possibly due to a gage rosette failure at buckling.

Because these failed measurements cannot be correlated with the corresponding FEA results, none of the inner surface strains are shown, to ease interpretation of the shell outer surface strains.
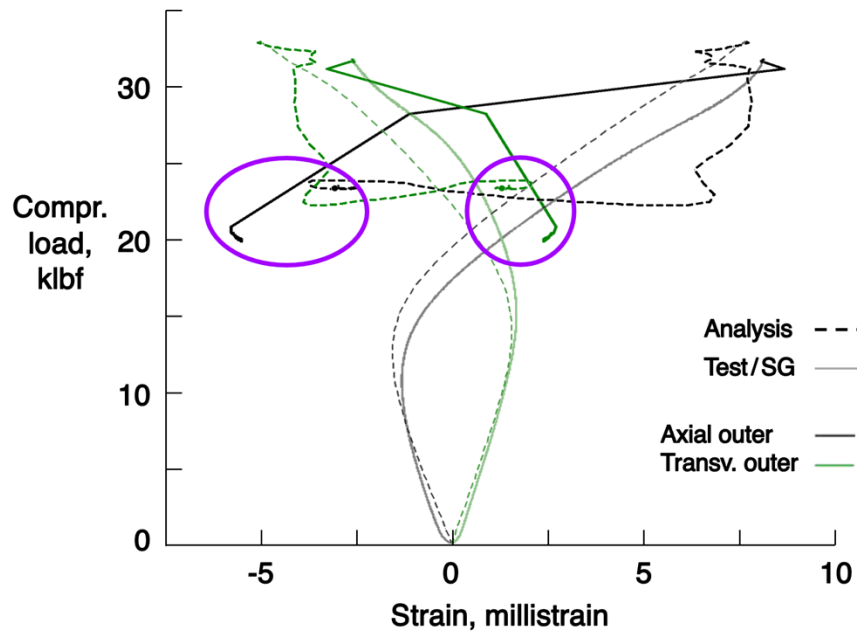

Figure 10b. Postbuckling strains at cutout left edge

The axial and transverse strain postbuckling paths on the shell outer surface, indicated by the heavier black and green lines in the figure, respectively, show good qualitative agreement in their trends from global buckling to stable postbuckling. As indicated within the purple circles, the strains at the stable postbuckling load also show very good quantitative agreement, and especially for the shell outer surface transverse strains. The overall agreement between these analytical and measured shell outer surface strains is assessed to be very good.

VI. Shell without overlaps

The analytical and measured structural responses of the shell without overlaps and a small cutout are plotted and discussed in this section. These comparisons are made at the center of the shell crown, and at the middle of the top and left edges of the cutout (Fig. 2). As described above for the shell with overlaps, similar refinements to the analysis step size were made here for the shell without overlaps. The analytical load-end shortening path for this shell without overlaps is unchanged from the results in Ref. 10, and is therefore not presented here. The analytical and measured stable postbuckling loads for this shell are 10,230 and 10,070 lbf, respectively.

In comparison to the shell with overlaps results reported above, the analytical deflections and strains for the shell without overlaps are highly symmetrical about a vertical plane bisecting the cutout (*i.e.*, left to right in Fig. 1a). Because nearly identical results are observed for this shell's crown and keel in prebuckling through stable postbuckling, only the crown results are presented and discussed here. No radial LVDT measurements were taken for this shell.

A. Crown center

Full-field, color contour plots of the nonlinear FEA and experimental DIC radial deflections of the regions surrounding the crown of the shell without overlaps are plotted at global buckling

and stable postbuckling in Fig. 11. As noted above for the shell with overlaps, the areas enclosed within these FEA and DIC images are different. Despite this, the qualitative postbuckling displacement patterns agree very well, with a single, deep radial depression noted in both test and analysis. Multiple shallow axial waves are oriented along the shell crown at global buckling in Fig. 11b. These inwardly oriented dimples are elliptical, with their major axes in the shell circumferential direction. The noise floors for the crown DIC measurements on the shell without overlaps are the same as reported above for the shell with overlaps.
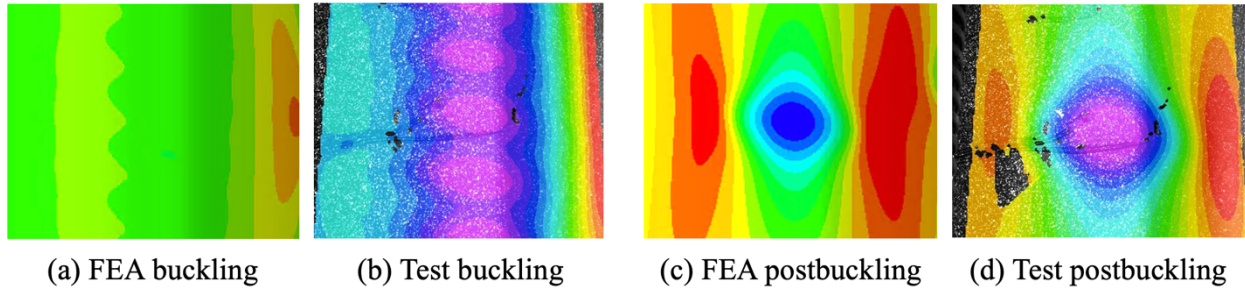

(a) FEA buckling   (b) Test buckling   (c) FEA postbuckling   (d) Test postbuckling

Figure 11. Full-field radial deflections around crown

1. Radial deflections

The nonlinear FEA and measured DIC radial deflections at the center of the crown of the shell without overlaps are plotted versus axial compression load in prebuckling up to global buckling in Fig. 12a. Displacements are plotted here for both the nonlinear FEA and deflections from the DIC measurements performed on the shell outer surface. As for the shell with overlaps, the crown and keel FEA deflections are identical, and no keel DIC observations were made. The FEA and DIC measurements differ slightly at lower loads, and then diverge rapidly as the axial load increases. The overall qualitative correlation across these results is fair, with poor quantitative agreement.
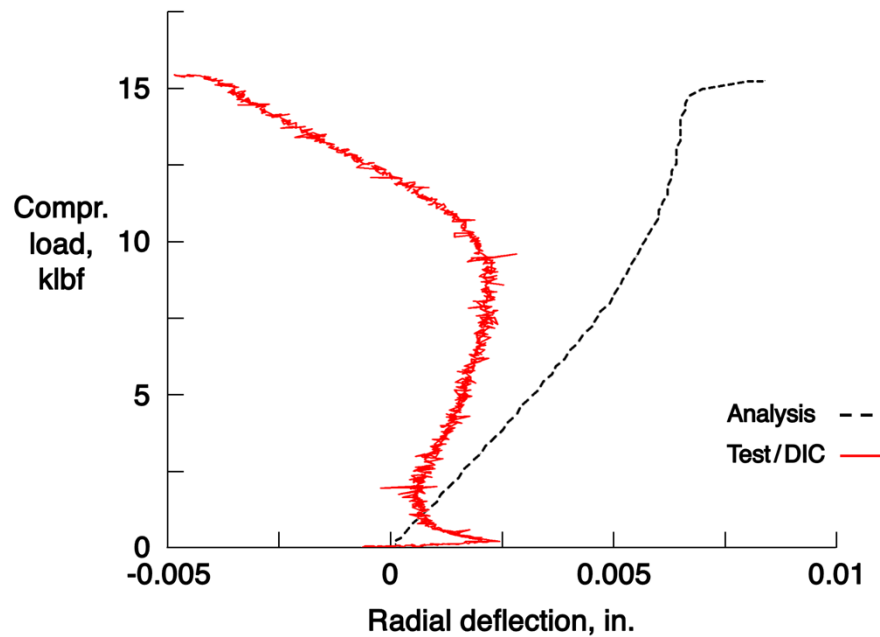

Figure 12a. Prebuckling deflections at crown center

American Institute of Aeronautics and Astronautics

The radial deflections at the center of the crown of the shell without overlaps are plotted versus axial compression load between global buckling and stable postbuckling in Fig. 12b. The qualitative correlation between these postbuckling paths is excellent, and the quantitative agreement between the final displacements at the stable postbuckled state (indicated within the purple circle) is very good. The analytical displacements on the shell crown (designated as the black dashed line) grow rapidly to a maximum amplitude of approximately 0.625 inches. For comparison on a quantitative basis, the DIC displacements at the stable postbuckling load reach a 0.5-inch amplitude at the stable postbuckled state, which is a 22 percent difference. Overall, the qualitative and quantitative agreement across these results is very good to excellent.
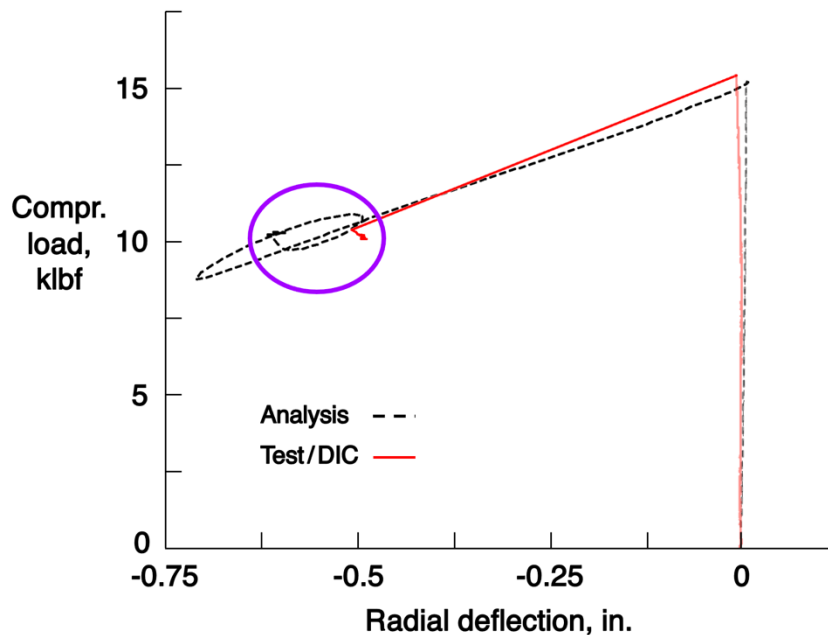

Figure 12b. Postbuckling deflections at crown center

2. Axial and transverse strains

The axial and transverse strains at the center of the crown of the shell without overlaps are plotted versus axial compression load in prebuckling up to global buckling in Fig. 13a. The nonlinear FEA, back-to-back strain gage measurements, and strains extracted from full-field DIC measurements on the shell outer surface shown are all highly linear, with minimal differences noted between the back-to-back results (*i.e.*, minimal local bending).

The analysis strains rapidly become nonlinear and asymptotic at higher loads, indicating the rapid onset of local bending at global buckling. The measured strains also show slight indications of nonlinearity at higher loads. Neglecting these nonlinearities, the coefficients of variation computed for the linear best-fit slopes are 6.2 and 2.9 percent for the axial and transverse strains, respectively. The correlation between test data and analyses is excellent for the results shown in this figure.

Postbuckling strains at the center of the shell without overlaps crown are plotted versus load in Fig. 13b. The nonlinear FEA and strains extracted from full-field DIC measurements on the shell outer surface are shown below. The experimental and analytical DIC postbuckling strain paths for the transverse strains (the green lines) compare well both qualitatively and quantitatively. The quantitative agreement between these final strains at the stable postbuckled state (indicated

within the purple circle) is excellent, with excellent overall qualitative and quantitative agreement between the transverse strains. However, the correlation for the corresponding postbuckling axial strain paths and final values is poor.
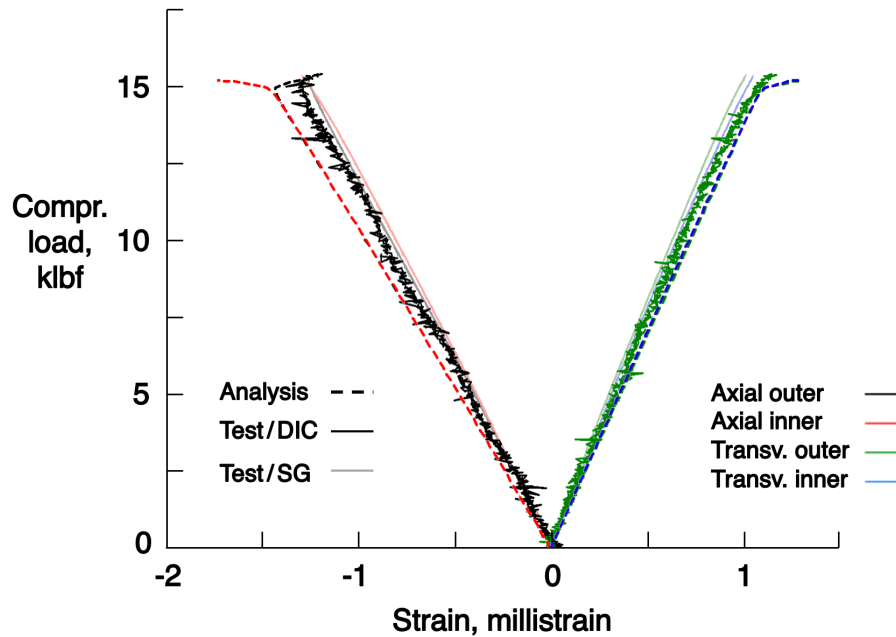

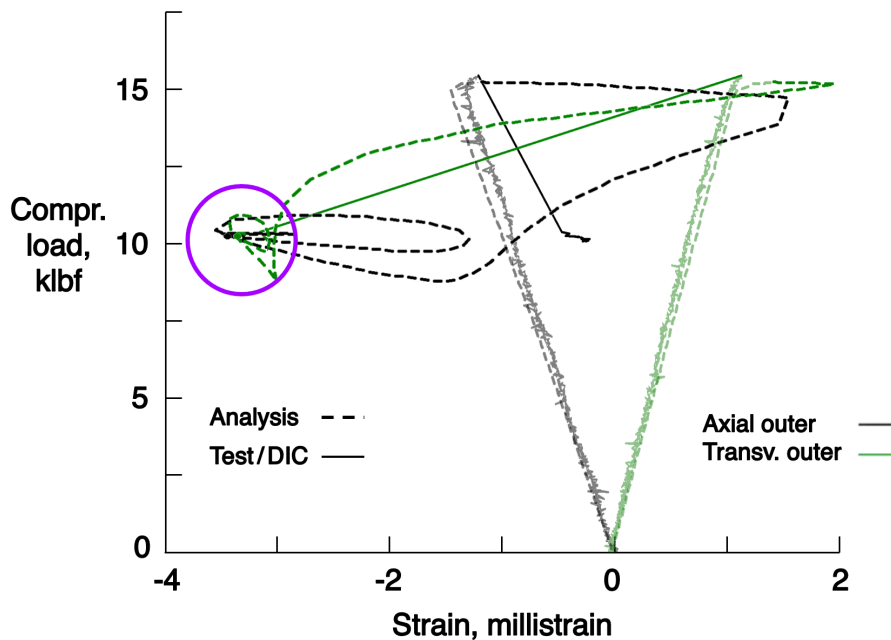**Figure 13a. Prebuckling strains at crown center**

Figure 13b. Postbuckling DIC strains at crown center

The axial and transverse strains at the center of the shell without overlaps' crown are plotted versus axial compression load between global buckling and stable postbuckling in Fig. 13c. Results are plotted here for the nonlinear FEA and back-to-back strain gage measurements. The averaged

back-to-back axial strain values are nearly zero at stable postbuckling, which corresponds well with the expectation of low in-plane axial loads in the postbuckled shell wall. The corresponding average transverse strains are approximately –0.5 millistrain, indicating that the shell has some circumferential membrane compression load after buckling. The differences between outer and inner surface postbuckling strains are large, indicating that the shell wall undergoes significant local bending at that location. This result also implies the presence of large radial deflections at the shell crown center, which are also plotted in Fig. 12b.
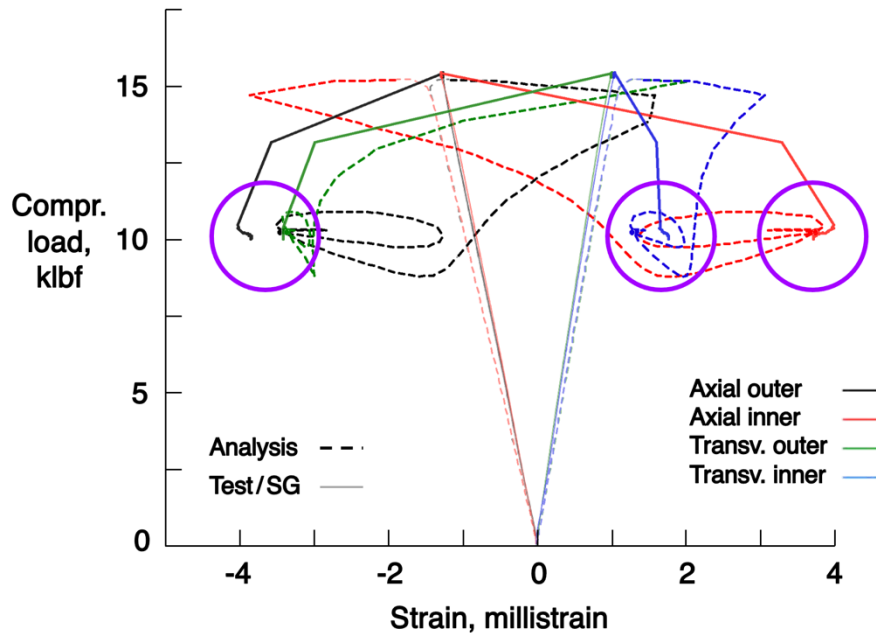

Figure 13c. Postbuckling gage strains at crown center

The measured and analytical axial and transverse strains on the shell outer and inner surfaces show very good agreement. Qualitatively, the axial and transverse postbuckling paths show good agreement. All of the measured and analytical strains show excellent quantitative agreement at stable postbuckling, as indicated within the purple circles. Overall, the qualitative and quantitative agreement between these postbuckling strain results is very good to excellent. However, while the transverse outer surface DIC and strain gage strains agree well, the axial outer results do not match, with the DIC magnitudes being much smaller than the gage strains.

B. Cutout top edge

Full-field, color contour plots of the nonlinear FEA and experimental DIC radial deflections around the cutout of the shell without overlaps are plotted at global buckling and stable postbuckling in Fig. 14. Qualitatively, the global buckling results agree very well, with different displacement patterns between analysis and test noted at the stable postbuckling state. As described above for the shell with overlaps, the DIC strain data around the cutout was extremely noisy with false artifacts (correlation issues) within the data set, and are therefore not presented here. Noise floors for the cutout DIC system on the shell without overlaps were also computed. The reported noise floor for the normal deflections is ±0.001 inches, and the maximum in-plane strain noise floor is ±0.310 millistrain.
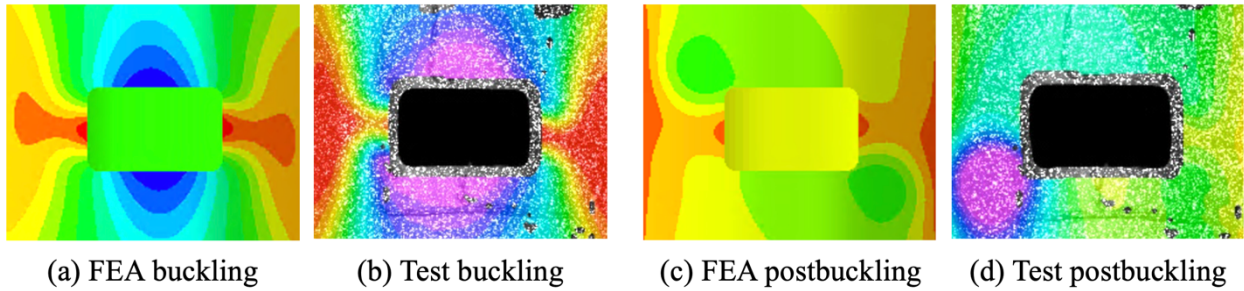
(a) FEA buckling   (b) Test buckling   (c) FEA postbuckling   (d) Test postbuckling

Figure 14. Full-field radial deflections around cutout

1. Radial deflections

The radial deflections at the middle of the cutout top edge of the shell without overlaps are plotted versus axial compression load in prebuckling up to global buckling in Fig. 15a. Results are plotted for the nonlinear FEA and displacements extracted from full-field DIC measurements on the shell outer surface. The FEA and DIC measurements are approximately linear with increasing load, reaching a maximum amplitude of about 0.16 inches, or 3.3 percent of the cutout circumferential dimension. The deflections differ slightly at lower loads, with the correlation improving as the axial load approaches global buckling. Overall, the qualitative and quantitative agreement across these results is excellent.

The postbuckling nonlinear FEA and measured DIC radial deflections for the shell without overlaps at the cutout top edge are plotted versus axial load in Fig. 15b. Qualitative comparison of the initial analytical and experimental postbuckling radial deflection paths plotted here show good correlation after global buckling, as indicated by the dashed purple circle. However, the qualitative agreement between these displacements at the stable postbuckling load is poor, with the FEA predicting a radial deflection of about 0.12 inches magnitude, as compared with the experimental magnitude of 0.19 inches. Overall, the qualitative and quantitative agreement across these postbuckling results is poor to fair.
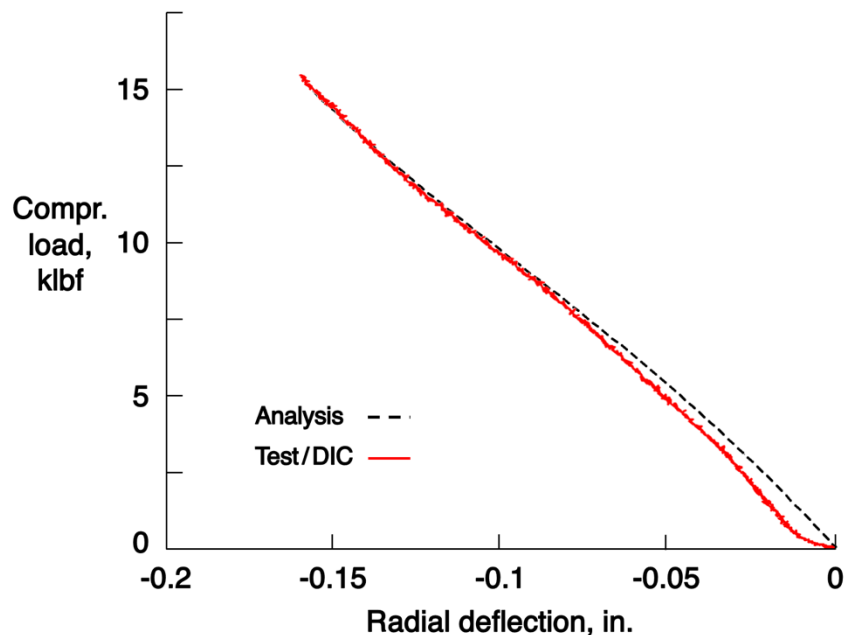

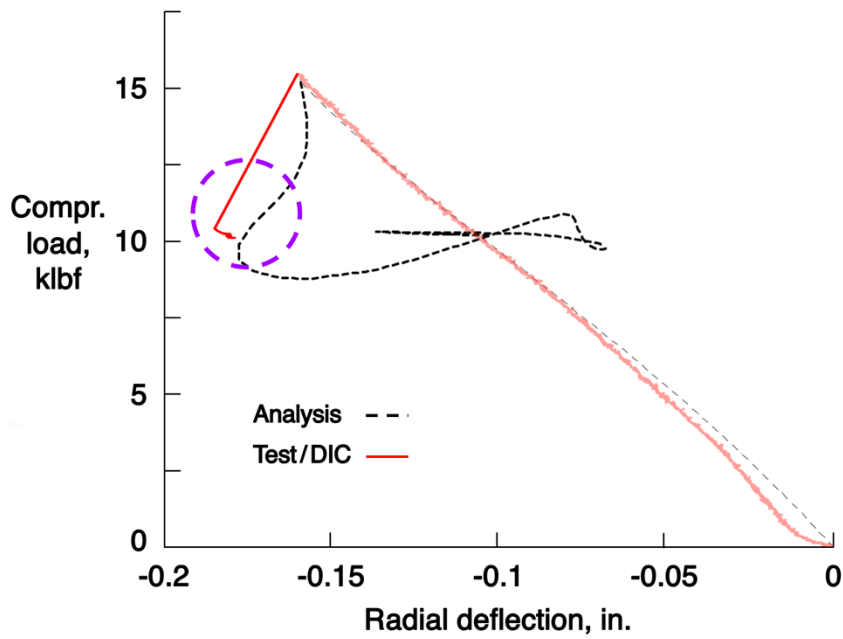**Figure 15a. Prebuckling deflections at cutout top edge**

Figure 15b. Postbuckling deflections at cutout top edge

2. Axial and transverse strains

The axial and transverse strains at the middle of the cutout top edge of the shell without overlaps are plotted in prebuckling up to global buckling versus axial load in Fig. 16a. Results are plotted for the nonlinear FEA and back-to-back strain gage measurements. The average strains from the back-to-back gage pairs are nearly zero, which indicates that the membrane forces are small at this location. The individual strains shown are nonlinear, with increasing differences between the back-to-back strain pairs indicative of increasing through-thickness bending with increasing load. Overall, the correlation across these results is excellent.
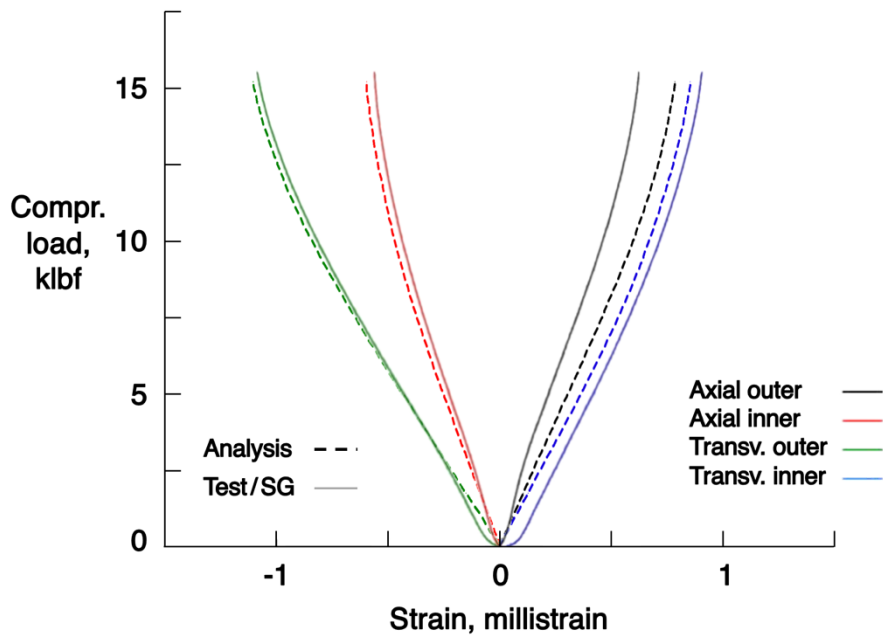

Figure 16a. Prebuckling strains at cutout top edge

American Institute of Aeronautics and Astronautics

The postbuckling axial and transverse strains on the shell without overlaps' cutout top edge are plotted versus axial compression load in Fig. 16b. The measured axial and transverse initial postbuckling paths drop sharply at global buckling to their stable postbuckling values. The initial analytical postbuckling paths show very good agreement (indicated by the dashed purple circles), but then rapidly approach zero at stable postbuckling. The measured and predicted strains at stable postbuckling do not agree as well, with the test strain magnitudes being approximately two times as large as the FE results. Therefore, the overall qualitative and quantitative agreement between the postbuckling strain results is assessed to be good to very good.
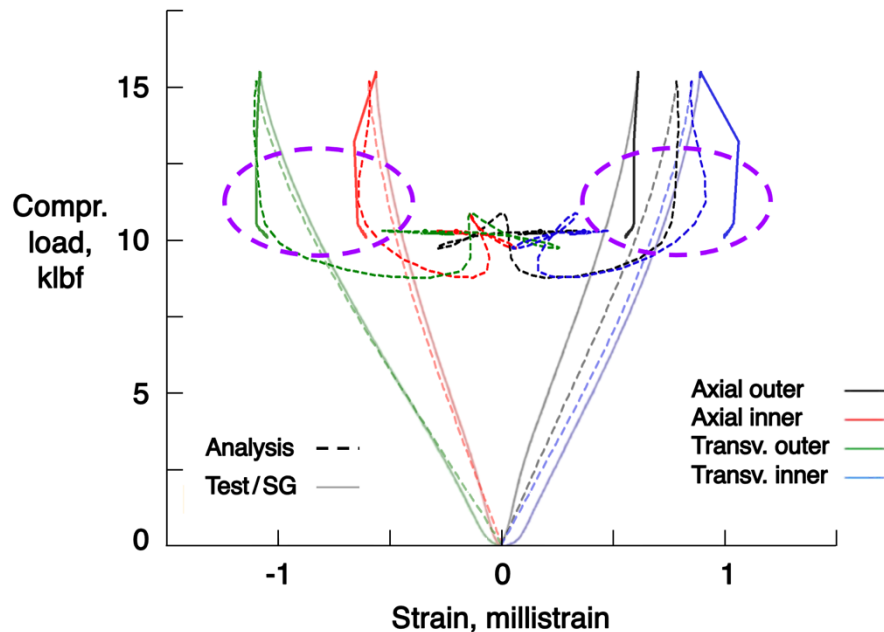

Figure 16b. Postbuckling strains at cutout top edge

C. Cutout left edge

1. Radial deflections

The prebuckling nonlinear FEA and measured DIC radial deflections at the shell without overlaps' cutout left edge are plotted versus axial load in Fig. 17a. The qualitative and quantitative correlation across these results is excellent, with all displacements increasing as the axial load increases. The DIC and FEA deflections show excellent agreement at lower loads, with gradually increasing deviation (less than 0.01 inches) at higher loads as the shell approaches global buckling. The maximum measured and analytical deflections of approximately 0.14 inches is 4.7 percent of the cutout axial dimension. Overall, the qualitative and quantitative agreement between these results is excellent.

The corresponding radial deflections at the middle of the cutout left edge of the shell without overlaps are plotted versus axial load between global buckling and stable postbuckling in Fig. 17b. Nonlinear FEA and measured DIC radial deflections are shown in this figure. Qualitative comparison of the initial analytical and experimental postbuckling radial deflection paths plotted here show some correlation after global buckling, with both deflections decreasing, but at different rates. Overall, these displacement paths and their values at the stable postbuckling load are in poor qualitative agreement.
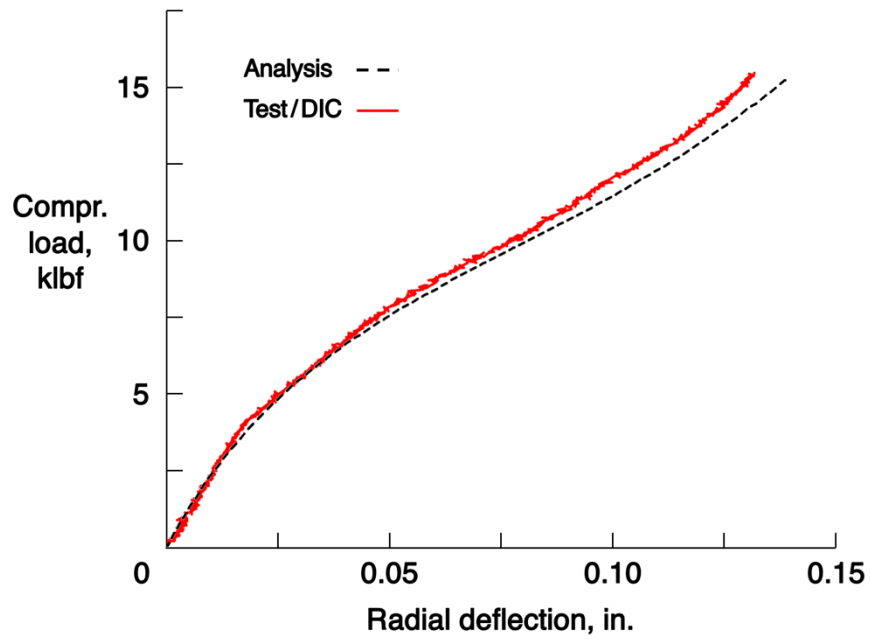
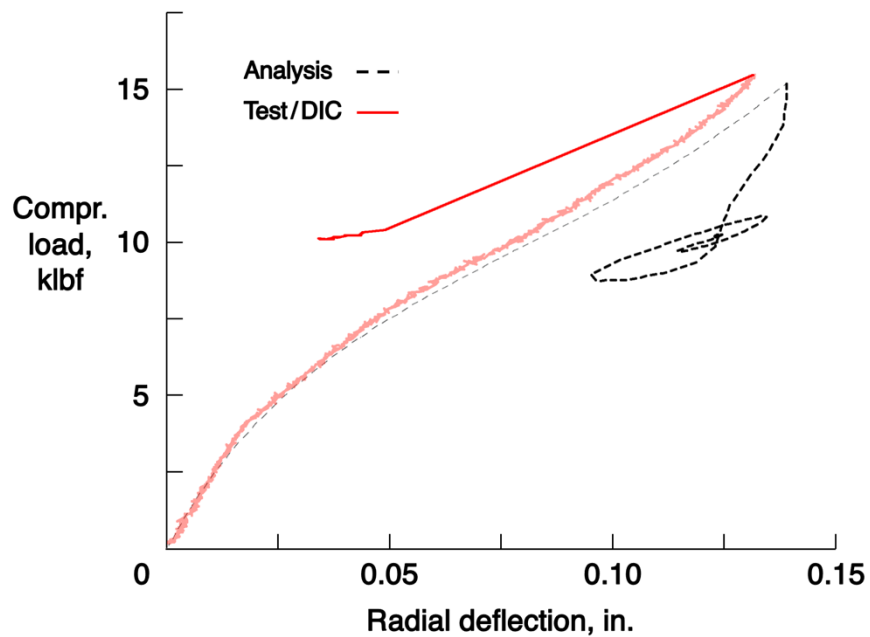**Figure 17a. Prebuckling deflections at cutout left edge**

Figure 17b. Postbuckling deflections at cutout left edge

2. Axial and transverse strains

Nonlinear FEA and back-to-back strain gage measurements at the middle of the shell without overlaps' cutout left edge are plotted in prebuckling up to global buckling versus axial compression load in Fig. 18a. The averaged strain magnitudes at the cutout edge increase to about 6 to 7 millistrain at global buckling, indicative of in-plane loading with increasing load. These axial and transverse strains are also nonlinear, with increasing differences between the back-to-back strain pairs corresponding to increasing through-thickness bending with increasing load. Overall, the correlation between measured and analytical results is excellent at this location.
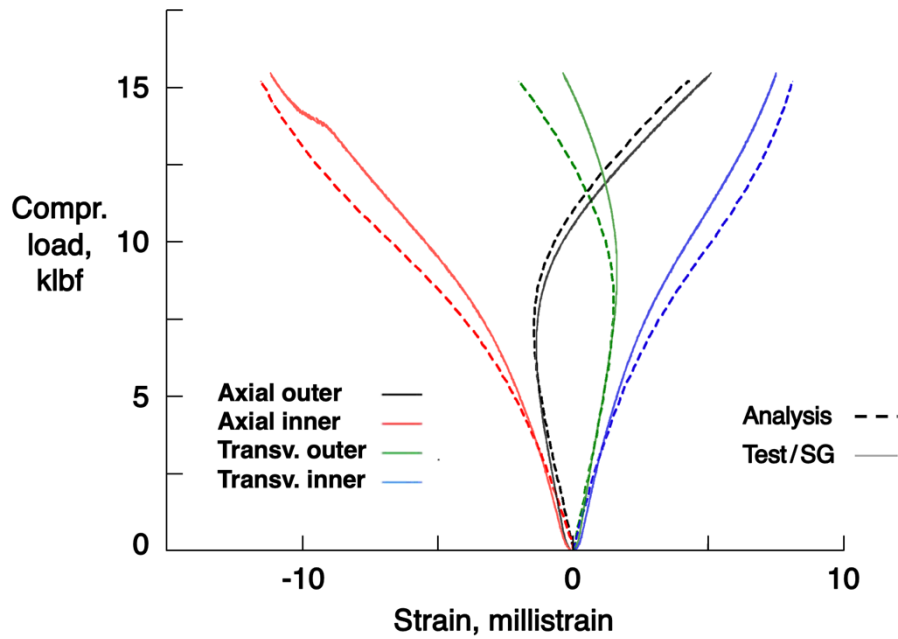
Figure 18a. Prebuckling strains at cutout left edge

The corresponding postbuckling axial and transverse strains on the shell without overlaps' cutout left edge are plotted versus axial load in Fig. 18b. At global buckling, the measured and analytical strains on the shell outer and inner surfaces all drop sharply, and equilibrate at approximately the same values at the stable postbuckling load. The postbuckling paths agree very well, with excellent quantitative agreement of the strains at the stable postbuckling load indicated within the purple circles. Overall, the qualitative and quantitative agreement between the results shown is very good to excellent.
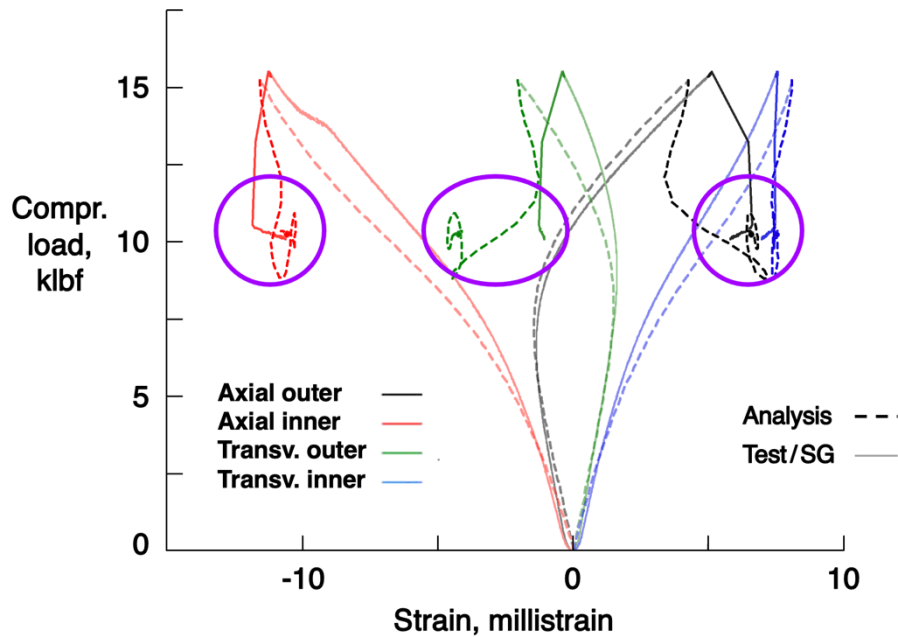

Figure 18b. Postbuckling strains at cutout left edge

American Institute of Aeronautics and Astronautics

VII. Discussion

Maximum compression strain amplitudes of between 5 and 15 millistrain are observed in several of the locations examined above, specifically the shell crown and keel, and cutout left edges. These approximate the average measured failure strains for the 16-ply laminates reported in Ref. 7 (–5.2 millistrain for a unidirectional laminate, and –13 millistrain for a cross-ply laminate). While this suggests that local material failures may have occurred within the shell walls, none of the typical indicators of material failure (*i.e.*, small, sudden discontinuities in deflection, strain, or load) are noted in the test results presented above. This latter point reinforces the results of the post-test thermography inspections of these shells, which indicated that no material failure had occurred.

The prebuckling FEA and DIC radial deflections at the centers of both shell's crowns show poor qualitative correlation. However, the DIC strains at that location, which are computed from the DIC displacements using the VIC-3D software, compare reasonably well with their analytical values up to global buckling, especially given their small magnitudes. One possible rationale for this apparent contradiction is that the DIC technique is better able to resolve the in-plane strain values, and cannot resolve the low prebuckling deflections normal to the shell wall (*i.e.,* towards and away from the cameras).

In comparison, the larger FEA and DIC radial deflections around the cutout edges show overall excellent qualitative correlation in prebuckling and up to global buckling, and in some cases even up to stable postbuckling. The DIC strains around the cutout edges were computed but were not presented here as they were found to have extremely poor correlation with the FEA results and experimental strain gage data. Possible rationales for this apparent contradiction are the multiple error sources at these locations that degrade reasonable correlation with strain gage measurements and analytical results include the physical cutout edge, the strain gage wire bundles, and coarse speckle pattern on the shell outer surface.

Table 1 presents a summary of the comparisons of the analytical and experimental deflections and strains described in the figures above. The cases with very good to excellent correlation are indicated in green, cases with poor to fair correlation in red, and partial correlation in yellow. Overall, the majority of the cases show very good to excellent qualitative and quantitative correlation, with equal numbers of cases with partial or no correlation.

		Shell with overlaps		Shell without overlaps	
		Prebuckling	Postbuckling	Prebuckling	Postbuckling
Crown	Defl./DIC	No	Yes	No	Yes
	Strain/DIC	Yes	Yes	Yes	Partial
	Strain/SG	Yes	Yes	Yes	Yes
Keel	Strain/SG	Yes	Yes	N/a	N/a
Cutout top	Defl./DIC	Yes	Partial	Yes	Partial
	Strain/SG	Yes	No	Yes	Partial
Cutout left	Defl./DIC	Yes	Yes	Yes	No
	Defl./LVDT	Yes	Yes	N/a	N/a
	Strain/SG	Yes	Yes	Yes	Yes

Table 1. Summary of analysis-test correlation

VIII. Concluding remarks

Experimental and analytical results for local radial deflections, axial strains, and transverse strains are plotted against axial compression load and compared for two tow-steered composite shells with small, unreinforced cutouts. These results are generated and compared at several discrete locations on the shell surface; the centers of the crown and keel (for the shell with overlaps), and two locations on the cutout perimeter.

The overall correlation between experimental and analytical results is excellent in prebuckling up to global buckling for both shells at all locations evaluated. In addition, the correlation from global buckling to stable postbuckling is very good, both qualitatively and quantitatively, in most cases for both shells evaluated in this study. This agreement for these postbuckling results is somewhat surprising, especially given the highly dynamic transition between global buckling and stable postbuckling, and the sparse strain gage data generated during that short time interval.

The structural performance of two tow-steered composite shells has been evaluated in this and previous studies (e.g., Refs. 7-10) both without and with cutouts. Experimental assessments of these shells have demonstrated that these small and large cutouts have relatively small impacts on their axial stiffnesses and global buckling loads. Extensive linear and nonlinear FEA have also been performed on these shells, showing very good overall agreement with the test results. These studies demonstrate the high potential of tow steering to mitigate the adverse effects of cutouts in axially loaded shells.

Acknowledgments

References

1.   D. H.-J. A. Lukaszewicz, C. Ward, and K. D. Potter: *The Engineering Aspects of Automated Prepreg Layup: History, Present and Future. Composites Part B: Engineering*, vol. 43, pp. 997-1009, 2012.

2.   B. C. Kim, K. Potter, and P. M. Weaver: *Continuous Tow Shearing for Manufacturing Variable Angle Tow Composites*. Composites Part A: Applied Science and Manufacturing, vol. 43, pp. 1347-1356, 2012.

3.   M. W. Hyer and H. H. Lee: *The Use of Curvilinear Fiber Format to Improve Buckling Resistance of Composite Plates with Central Circular Holes*. Composite Structures, Vol. 18, No. 3, 1991.

4.   B. F. Tatting and Z. Gürdal: *Design and Manufacture of Elastically Tailored Tow Placed Plates*. NASA/CR-2002-211919, August 2002.

5.   K. C. Wu: *Design and Analysis of Tow-Steered Composite Shells Using Fiber Placement*. Proceedings of the ASC 23rd Annual Technical Conference. Memphis, Tennessee, September 9-11, 2008. Paper no. 125.

6.   K. C. Wu, B. F. Tatting, B. H. Smith, R. S. Stevens, G. P. Occhipinti, J. B. Swift, D. C. Achary, and R. P. Thornburgh: *Design and Manufacturing of Tow-Steered Composite Shells Using Fiber Placement*. Proceedings of the 50th AIAA/ASME/ASCE/AHS/ASC Structures, Structural Dynamics and Materials Conference. Palm Springs, California, May 4-7, 2009. Paper no. AIAA 2009-2700.

7.   K. C. Wu, B. K. Stanford, G. A. Hrinda, Z. Wang, R. A. Martin, and H. A. Kim: *Structural Assessment of Advanced Composite Tow-Steered Shells*. Proceedings of the 54th

AIAA/ASME/ASCE/AHS/ASC Structures, Structural Dynamics and Materials Conference. Boston, Massachusetts, April 8-11, 2013. Paper no. AIAA 2013-1769.

8. S. C. White, P. M. Weaver, and K. C. Wu: *Post-Buckling Analyses of Variable-Stiffness Composite Cylinders in Axial Compression*. Composite Structures, Vol. 123, May 2015. Pages 190-203.

9. K. C. Wu, J. D. Turpin, B. K. Stanford, and R. A. Martin: *Structural Performance of Advanced Composite Tow-Steered Shells with Cutouts*. Proceedings of the 2014 AIAA Science and Technology Forum and Exposition. National Harbor, Maryland, January 13-17, 2014. Paper no. AIAA 2014-1056.

10. R. M. J. Groh and K. C. Wu: *Nonlinear Buckling and Postbuckling Analysis of Tow-Steered Composite Cylinders with Cutouts*. AIAA Journal, June 2022. https://doi.org/10.2514/1.J061755

11. M. A. Sutton, J.-J. Orteu and H. W. Schreier: *Image Correlation for Shape, Motion and Deformation Measurements: Basic Concepts, Theory, and Applications*. Springer, 2009.

12. International Digital Image Correlation Society, E. M. C. Jones and M. A. Iadicola (eds.). *A Good Practices Guide for Digital Image Correlation*, 2018. https://doi.org/10.32720/idics/gpg.ed1

13. *Abaqus 2018 User's Manual*, Dassault Systèmes SIMULIA Corporation, Providence, Rhode Island. 2018.

14. R. M. Neville, R. M. J. Groh, A. Pirrera, and M. Schenk: *Beyond the Fold: Experimentally Traversing Limit Points in Nonlinear Structures.* Proc. R. Soc. A 476: 20190576. https://doi.org/10.1098/rspa.2019.0576